Volume 24
Number 19
7 October 2024
Pages 4473–4670

Lab on a Chip

Devices and applications at the micro- and nanoscale

rsc.li/loc

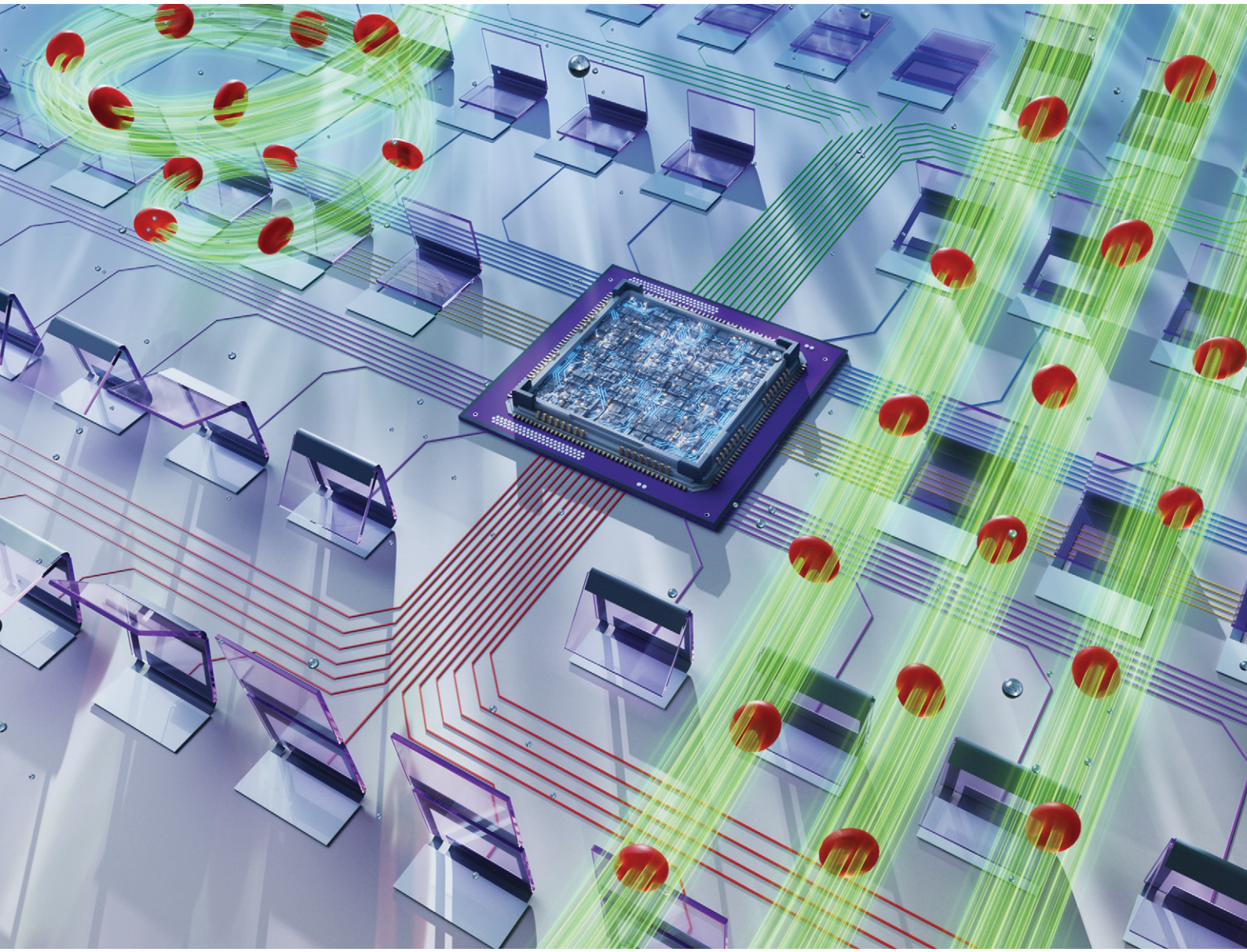

ISSN 1473-0197

ROYAL SOCIETY OF CHEMISTRY

PAPER
Wei Wang, Itai Cohen *et al.*
Electronically actuated artificial hinged cilia for efficient bidirectional pumping

Lab on a Chip

PAPER

View Article Online
View Journal | View Issue

Check for updates

Cite this: *Lab Chip*, 2024, **24**, 4549

Electronically actuated artificial hinged cilia for efficient bidirectional pumping†

Wei Wang, *[abc] Ivan Tanasijevic, [de] Jinsong Zhang, [a] Eric Lauga [d] and Itai Cohen *[acfg]

Cilial pumping is a potent mechanism used to control and manipulate fluids on microscales. Recently, we introduced an electronically driven μ-cilial platform that can create arbitrary flow patterns in liquids near a surface with the potential for various engineering applications. This μ-cilial platform, however, utilized the coupling between elasticity and viscous drag to obtain pumping and had several limitations. For example, each cilium could only pump in one direction. Thus, to create bidirectional flows, it was necessary to fabricate and separately actuate two oppositely facing cilia. As another example, the generation of non-reciprocal cilial motions, a necessary condition for pumping at these scales, could only be achieved by matching the elastic stresses inherent in actuating the cilia with the viscous drag forces generated by the flows. This criterion severely restricted the frequency range over which the cilia could be operated and resulted in a small swept area, both of which restricted the volume of fluid being pumped in each cycle. These limitations contrast with the capabilities of natural cilia, which can achieve omnidirectional transport and operation over a broad range of frequencies. In natural cilia, these capabilities arise from their complex internal structure. Inspired by this strategy we designed hinged cilia and show they can achieve bidirectional pumping of larger fluid volumes over a broad range of frequencies. Finally, we demonstrate that even regular arrays of individually controlled hinged cilia can generate a variety of flow patterns using fewer cilia than in previous cilia metasurface designs.

Received 14th June 2024,
Accepted 20th August 2024

DOI: 10.1039/d4lc00513a

rsc.li/loc

Open Access Article. Published on 22 August 2024. Downloaded on 9/11/2025 10:19:27 AM.
This article is licensed under a Creative Commons Attribution-NonCommercial 3.0 Unported Licence.

1 Introduction

Microorganisms often employ non-reciprocal cilial and flagellar beating as their primary means of propelling fluids to great effect.[1–5] For instance, cilia in the respiratory system of humans, are less than 10 μm long, yet pump mucus with a speed of about 500 μm s^{-1}.[6] Inspired by these capabilities, significant efforts have been dedicated to the development of artificial cilia and flagella for applications in swimming and fluid pumping.[7–12] Recently, we introduced a promising electronically actuated artificial cilial platform that uses surface electrochemical actuators (SEAs)[13,14] to drive individually addressable artificial cilia and showed that surfaces patterned with these cilia could generate programmable flow patterns.[15]

Despite its successes, this platform had several limitations stemming from the fact that, to pump fluid, the cilia had to take advantage of coupling between the internal elastic stresses and viscous drag forces arising from the induced flows. This coupling resulted in several constraints. First, this coupling mechanism sets the pumping direction. The elastic force and viscous drag change along the cilia, making the deformation most pronounced at the tip. This mechanism produced a uni-directional fluid flow moving from the fixed root to the cilia tip.[15] To achieve bidirectional pumping, it is necessary to selectively actuate oppositely-orientated cilia. In addition, to produce significant asymmetry between the forward and backward strokes, a necessary condition for pumping fluids at these low Reynolds numbers, the actuation timescale must be comparable to the cilia's natural deformation timescale, a condition that occurs only for a select ranges of frequencies, 10–100 Hz.[15] Moreover, the extent of the overall deformation, and thus, the pumping efficacy, results from the complex interplay between the periodic internal actuation and the viscosity-limited

[a] *Laboratory of Atomic and Solid State Physics, Cornell University, Ithaca, New York, 14850, USA. E-mail: ww459@cornell.edu, itai.cohen@cornell.edu*
[b] *Sibley School of Mechanical and Aerospace Engineering, Cornell University, Ithaca, New York, 14850, USA*
[c] *Kavli Institute at Cornell for Nanoscale Science, Cornell University, Ithaca, New York, 14850, USA*
[d] *Department of Applied Mathematics and Theoretical Physics, University of Cambridge, Cambridge, CB3 0WA, UK*
[e] *The Institute for Artificial Intelligence Research and Development of Serbia, Serbia*
[f] *Department of Physics, Cornell University, Ithaca, New York, 14850, USA*
[g] *Department of Design Technology, Cornell University, Ithaca, New York, 14850, USA*

† Electronic supplementary information (ESI) available. See DOI: https://doi.org/10.1039/d4lc00513a

Open Access Article. Published on 22 August 2024. Downloaded on 9/11/2025 10:19:27 AM.
This article is licensed under a Creative Commons Attribution-NonCommercial 3.0 Unported Licence.

propagation of deformation from the free-end (tip) to the anchored root. This is clearly a much higher-order mechanism than forcing the deformation and, in turn, generates a small pumping distance per actuation cycle of about 2 μm, with a maximal pumping speed of about 60 μm s^{-1}.[15] Developing new artificial cilia that can overcome these limitations would significantly improve the function of cilial metasurfaces.

Remarkably, the actuated cilia and flagella in living organisms do not suffer from these limitations. The intricate structure of motile cilia, is typically characterized by nine microtubules surrounding two internal microtubules.[16] Dynein ATPase motor proteins are used to generate relative sliding between adjacent microtubules, which deforms the cilia enabling them to achieve non-reciprocal trajectories with large swept areas, efficient pumping across a broad range of frequencies, and versatile trajectories for pumping and swimming.[16] Similarly, bacterial flagella use motors and rotors to generate flagella rotation and achieve nonreciprocal trajectories.[17] Such capabilities enable these organisms to adapt to various micro environments. For example, bacteria such as *Escherichia coli* are able to climb chemical gradients by periodically reversing the direction of flagella rotation to generate 'run-and-tumble' motions,[18–20] and *Paramecium* cells can tune their cilia beating frequency to change the swimming speed to rheotaxis and implement avoidance behaviors.[21,22] The key to achieving these superior fluid manipulations is shape control *via* internal actuation.

Here, inspired by these natural systems, we introduce cilia with internal hinges that can adopt a series of distinct shapes. This design involves driving two hinges, one at the base, and one in the middle of each cilium using two phase-delayed oscillating signals. The cilia cycle between folded and extended shapes to generate non-reciprocal trajectories capable of inducing bidirectional fluid pumping over a broad range of frequencies (Fig. 1). This additional capability enables us to achieve a diverse range fluid flows using fewer cilia than the previously reported platform.

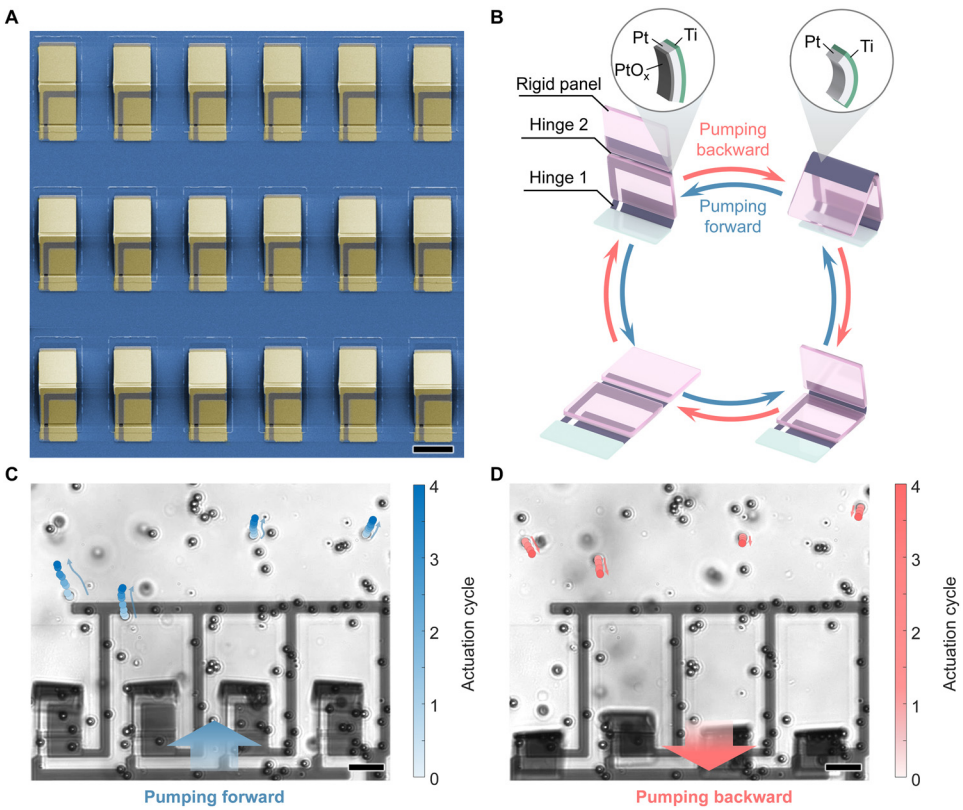

Fig. 1 Scanning electron microscope images and pumping mechanism of the hinged cilium. (A) A false-color scanning electron microscope image of the hinged cilia arrays. (B) The shape-shifting sequences of the hinged cilium. Each cilium consists of two independently controllable hinges. We incorporate a secondary wire passing through the first hinge (Hinge 1) to activate the second hinge (Hinge 2). The cilium is made of the surface electrochemical actuators[13–15] with 7 nm Pt and 3 nm Ti. The two top insets show the actuation of the actuator. The actuator is bent up due to prestress from fabrication. The exposed Pt surface oxidizes into PtO_x and expands under a positive voltage of ~1 V and flattens the actuator (left inset), and the PtO_x reduces under a negative voltage of ~−0.5 V and, in turn, bends the actuator (right inset). The cilium adopts these four shapes clockwise with a positive phase delay of Hinge 2 and counterclockwise with a negative Hinge 2 phase delay. These two cases result in two opposite pumping directions as they generate swept areas with opposite signs. (C) and (D) The bidirectional pumping of a hinged cilia array with four cilia. We highlight the movement of represented particles using changing colors. (C) The particle motions in the pumping forward case. (D) The particle motions in the pumping backward case. Scale bar: 25 μm.

 This journal is © The Royal Society of Chemistry 2024

Open Access Article. Published on 22 August 2024. Downloaded on 9/11/2025 10:19:27 AM.
This article is licensed under a Creative Commons Attribution-NonCommercial 3.0 Unported Licence.

2 Results

To construct our artificial cilia, we developed a fabrication technique that makes use of recently developed surface electrochemical actuators (SEAs).[13–15] In brief, one hinged cilium consists of two independently controllable hinges, each constructed from a 7 nm thick platinum (Pt) thin film, capped on the lower side by a 3 nm layer of titanium (Ti) (Fig. 1). The actuator bending is localized into hinges by 500 nm thick SiO_2 rigid panels (see Materials and methods and ESI† Fig. S1 for the fabrication process). A metal wire is threaded through Hinge 1 to enable independent control of Hinge 2. Arrays of hinged cilia are shown in Fig. 1A. To induce actuation of the artificial cilium in phosphate-buffered saline (PBS; 1×; pH 7.45), the actuator's potential is raised to approximately 1 V relative to the Ag/AgCl reference electrode, allowing the hydroxide ions to react with Pt and generate platinum oxide (PtO_x) and water. The oxide in Pt expands the Pt lattice, resulting in an extension strain on the Pt layer surface,[14] resulting in the flattening of the actuator (top left inset in Fig. 1). Subsequently, applying a voltage of approximately −0.5 V enables the PtO_x to react with water, generating hydroxide ions and reducing the PtO_x into Pt, restoring the actuator to its initial state (top right inset in Fig. 1B).

Applying two phase-delayed oscillating voltage signals to actuate the cilium allows the cilium to cyclically transit among four distinct shapes (Fig. 1B), facilitating the generation of nonreciprocal trajectories—an essential characteristic for inducing pumping in low Reynolds number environments.[23–25] In Fig. 1B, the cilium sequentially adopts these shapes in a clockwise fashion when Hinge 2 is driven using a positive phase delay relative to Hinge 1, and results in fluid pumping from the tip to the fixed root (pumping backward). Conversely, a counterclockwise shape shifting sequence occurs when Hinge 2 is driven with a negative phase delay relative to Hinge 1, leading to fluid movement from the fixed root to the tip (pumping forward). These two scenarios yield opposite pumping directions (refer to ESI† Video S1) due to the generation of swept areas with opposite signs (refer to the ESI† and Fig. S2 for details on the swept area). To provide a visual representation of the bidirectional

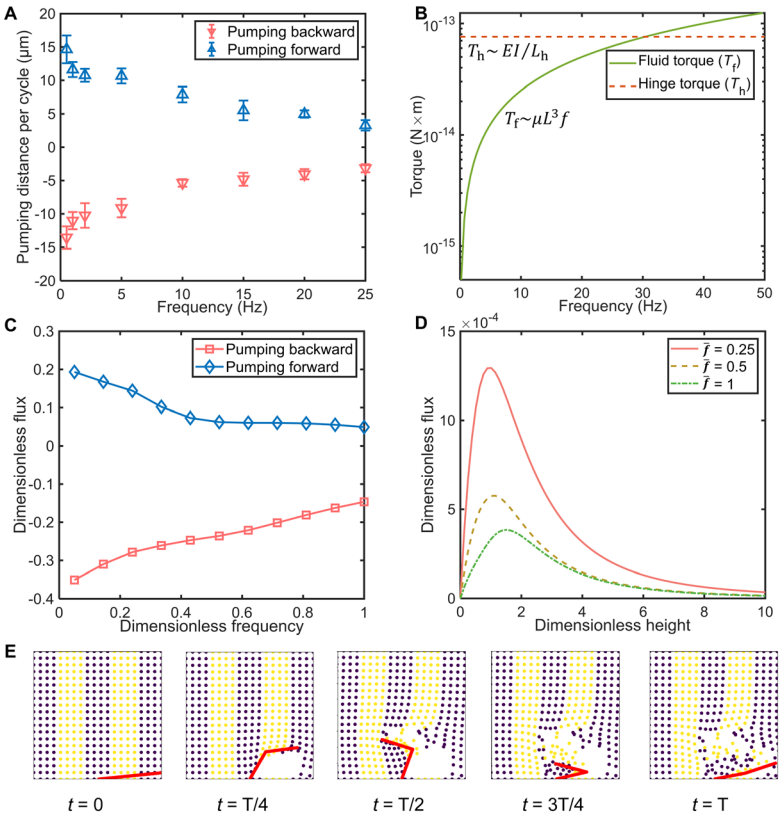

Fig. 2 Pumping of the hinged cilia. (A) Experimental pumping performance: the relationship between the pumping distance per actuation cycle and frequency. We observe a maximum pumping forward distance (defined as flow moving from the fixed root to the tip) of approximately 15 μm per cycle at 0.5 Hz, and an optimal pumping backward (defined as the flow moves from the tip to the fixed root) distance per cycle of approximately 14 μm at 0.5 Hz. (B) The analytical comparison between the fluid torque and hinge torque. (C) Simulation pumping performance: the relationship between the dimensionless frequency and the dimensionless flux per actuation cycle. (D) The simulated relationship between the dimensionless height and dimensionless flux at different dimensionless frequencies ($\bar{f}$). (E) The side view of the simulated flow displacement within one actuation cycle. We use alternating purple and yellow dots to illustrate the flow displacement. The sequence of images, from left to right, represents the flow displacement at various time intervals: t = 0, t = T/4, t = T/2, t = 3T/4, t = T, where T denotes the total duration of one actuation cycle.

Open Access Article. Published on 22 August 2024. Downloaded on 9/11/2025 10:19:27 AM.
This article is licensed under a Creative Commons Attribution-NonCommercial 3.0 Unported Licence.

pumping, we display the positions of the microparticles, denoted by colored circles, in Fig. 1C and D. Notably, the electronic signals driving the cilia can be applied either externally through wiring and probing for tethered control or internally through microscale CMOS circuits for untethered control (see ESI† Fig. S3, Materials and methods, and ref. 15 for details).

We assess the pumping performance of the hinged cilia by tracking the fluid motion, *via* tracer particles, during cilial actuation. Specifically, we vary the actuation frequency (from 0.5 Hz to 25 Hz) and monitor the pumping distance per cycle (Fig. 2A). Here, to get a uniform flow field, we use one cilia array consisting of four cilia, with a spacing of 50 μm, to measure the pumping performance. Each cilium has a width of 25 μm and a length of 50 μm. We find that the hinged cilia provide several advantages compared to the previous design. First, hinged cilia can achieve bidirectional pumping with comparable pumping performance (Fig. 2A, ESI† Video S1) by simply reversing the phase delay of the two input voltage signals. Second, we find that the hinged cilia can pump over a range of frequencies (0.5 Hz to 25 Hz) provided the viscous drag, which is proportional to velocity, is not dominant (Fig. 2A). Third, due to the large swept area of the hinged cilium (see ESI†), they obtain a peak pumping distance per cycle of about 15 μm and a peak pumping speed of about 100 μm s^{-1} (ESI† Fig. S4), significantly surpassing the performance of the previous design[15] whose maximal pumping distance is ~2 μm and maximal pumping speed is ~60 μm s^{-1}.

Intriguingly, we find that the pumping distance per actuation cycle decreases with the actuation frequency (Fig. 2A). We hypothesize that the interplay between hinge elasticity and fluid hydrodynamics explains this decreasing trend. Assuming that the kinematic and the cilia motion do not change with the frequency, the total viscous drag, which is proportional to velocity, also increases with actuation frequency. Since at micro-scales, the internal elastic stresses must overcome the fluid drag, the increase in frequency will reduce the deformation amplitude leading to decreased pumping distance per cycle. We can estimate the region where the viscous drag starts to influence the hinge actuation by comparing the magnitudes of the hinge torque and the viscous drag calculated for the full range of deformation. Specifically, we use beam theory to calculate the hinge torque and resort to fundamental low Reynolds number fluid mechanics to estimate the fluid torque (see ESI† and Fig. 2B). The hinge torque T_h is EI/L_h, where E is Young's modulus, I denotes the hinge's moment of inertia, and L_h is its length. The fluid torque at full deformation is estimated as $T_f \sim \mu L^3 f$, where μ is the viscosity, L is the cilium's length, and f is the actuation frequency. For the cilia dimensions tested in the current experiments (L = 50 μm, W = 25 μm), we find that the fluid drag at full deformation reaches the same order as the hinge stiffness at frequencies above 3 Hz (Fig. 2B), which is consistent with experimental data in Fig. 2(A) (see ESI† for details).

To further validate the suspected pumping mechanism, we develop a simple theoretical model that approximates the cilium as rigid rods connected by torsional springs and the fluid as Newtonian fluid with low-Reynolds number dynamics (see Materials and methods and ESI† Fig. S5 for details). Results of the numerical simulations of the model cilia (Fig. 2C) replicate the experimentally observed pumping behaviors (Fig. 2A). We note the similar decreasing trend between the pumping distance per cycle and actuation frequency in the simulated cilia as in the experimental results discussed above. Notably, the backward and forward flows are not symmetric. We hypothesize that this asymmetry arises from the nonlinear coupling between the hinge elasticity and the hydrodynamics.

In addition to resolving the origin of the frequency dependence, the simulation allows for obtaining the resulting flow profiles. Here, we plot the flux at different heights (Fig. 2D) and find that it reaches the peak amplitude at about the tip of the cilium and decreases along both sides of the height direction. Consistent with the frequency dependency in Fig. 2A and C, the peak flux decreases with frequency. To visualize the pumping profile within one actuation cycle, we plot the fluid motion *versus* actuation in Fig. 2E (ESI† Video S2) and use the displacement of alternative purple and yellow dots to represent the fluid motion. Overall, the experimental data, analytical estimates, and simulations highlight that phase-delayed actuation offers an effective way to actuate the hinged cilia producing large fluid displacements, non-reciprocal trajectories, and bidirectional pumping at the microscale.

The bidirectional pumping enabled by hinged cilia allows for creating programmable and intricate flow patterns even with a simple cilia configuration, such as a single array. To illustrate this idea, we fabricate a cilia array comprised of four cilia. We display various flow patterns that we achieved using this cilia array in Fig. 3. In each column, we show four images depicting the sequential shape-shifting during one actuation cycle at the top, with the red and blue arrows indicating the anticipated flow direction for each cilium. At the bottom, we show a composite image with both the experimental and simulated streamlines. The experimental streamlines obtained from tracking fluorescent tracer particles (depicted in white) are shown at the bottom of the composite images (see the pumping video in ESI† Video S3). Additionally, we employ four Stokeslets to simulate the cilia array and plot simulated flow 3D streamlines[26] (refer to Materials and methods for details) and velocity profile in the middle and show the depth-averaged simulation streamlines at the top. In the first column, we prescribe that all the cilia pump in the forward direction (Fig. 3A). In the second column, we prescribe that the left two cilia pump forwards and the right two cilia pump backwards, generating a flow vortex (Fig. 3B). In the third column, we prescribe that the left and right cilia pump forwards while the middle two cilia pump backwards, resulting in two vortices with opposite rotation directions (Fig. 3C). In all three instances, there is

 This journal is © The Royal Society of Chemistry 2024

Open Access Article. Published on 22 August 2024. Downloaded on 9/11/2025 10:19:27 AM.
This article is licensed under a Creative Commons Attribution-NonCommercial 3.0 Unported Licence.

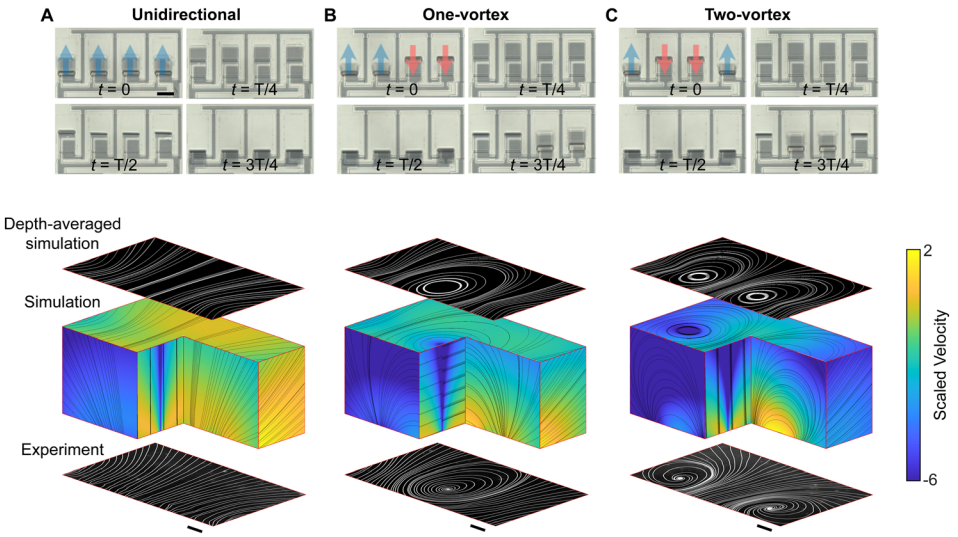

Fig. 3 Flow patterns of one cilia array comprising four hinged cilia. In each pattern, the top four subfigures show the shape-shifting sequence of the cilia at distinct times: t = 0, t = T/4, t = T/2, and t = 3T/4, where T is the total duration of one actuation cycle. We present a composite image below these images with the experimental streamlines at the bottom, the simulated 3D streamlines in the middle, and the depth-averaged simulated streamlines at the top. (A) Unidirectional pumping. (B) One vortex with clockwise rotation. (C) Two vortices with the left vortex rotating clockwise and the right vortex rotating counterclockwise. Scale bar: 25 μm.

excellent agreement between experimental and simulation results (ESI† Fig. S6). Notably, the same cilia array can be adapted to produce additional flow patterns as needed. For instance, reversing the vortex direction of the left/right vortex in Fig. 3C yields two vortices with the same direction of rotation. Such vortex designs allow for moving particles horizontally with vertical pumping (ESI† Video S4), enabling the generation of 2D flow patterns even as the cilia are constrained to pump along a single direction.

When multiple cilia arrays are combined, we are able to generate additional fluid manipulation capabilities and numerous functional flow patterns. In Fig. 4, we demonstrate

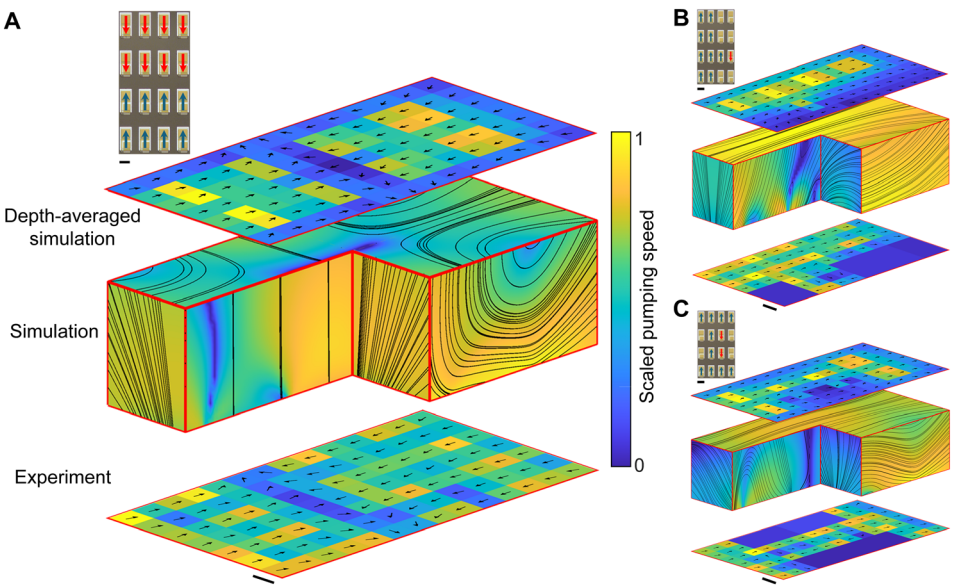

Fig. 4 Flow patterns from a hinged cilia surface. For each flow pattern, the experimental flow profile is presented at the bottom, where arrows indicate the flow directions and colors represent the relative amplitude (normalized by the maximal velocity). The simulated 3D streamlines and velocity are present in the middle, and the depth-averaged simulated velocity is shown at the top. The expected flow is highlighted in the top right, with the red and blue arrows showing the flow direction given by the hinged cilia. (A) Converging flow: the bottom two cilia arrays pump forward, and the top two backward, leading to a converging flow pattern. (B) Parallel transport and mixing: the right two cilia columns pump forward, with the left cilia creating a flow vortex, facilitating parallel transport and mixing. (C) Serial transport and mixing: the bottom cilia array pumps forward, with the middle two arrays generating a flow vortex, complemented by the forward pumping of the top cilia array. This arrangement supports a sequential transport and mixing process. Scale bar: 25 μm.

Open Access Article. Published on 22 August 2024. Downloaded on 9/11/2025 10:19:27 AM.
This article is licensed under a Creative Commons Attribution-NonCommercial 3.0 Unported Licence.

these additional capabilities using a cilia surface with a four by four cilial array. For each flow pattern in Fig. 4, we show the imposed cilial pumping pattern indicated *via* the blue and red arrows in the top left inset. We present the experimentally obtained flow field at the bottom, with the arrows showing the flow direction and the color showing the scaled pumping speed. We show the simulated 3D streamlines in the middle, and the simulated depth-averaged velocity field (see Materials and methods) at the top. In all our measurements, we find excellent agreement between the depth-averaged experimental, and simulation flow patterns. In Fig. 4A, we demonstrate the flow pattern that emerges from two converging flows. Here, two cilia arrays pump the fluid forward and two cilia arrays pump the fluid backward (see ESI† Video S5). The generated flows meet in the middle to generate an upwelling flow that also extends towards the left and right. In Fig. 4B, we demonstrate simultaneous fluid transport and mixing by letting the left two cilia columns pump forward while creating a fluid vortex on the right. Finally, in Fig. 4C, we demonstrate serial flow transport and mixing by first pumping the fluid forward, then mixing the fluid *via* two vortices, and then pumping the fluid forward again. As these examples illustrate there is a vast range of functional microflow patterns that can be generated with such cilia arrays, highlighting the great potential for using these hinged cilia to generate and manipulate fluids at the microscale.

3 Discussion

Collectively, these studies illustrate that cilia with internal hinges allow for generating non-reciprocal trajectories and efficient bidirectional pumping over a large actuation frequency range. Impressively, arrays of such cilia allow for generating the elementary flow geometries presented in previously reported platforms with fewer cilia and more elegant designs. As demonstrated, such designs can take advantage of vortices generated by oppositely pumping neighboring cilia to move particles forward, backward, or sideways. With just four cilia, it is also possible to generate sink, source, and extensional flows. Such elemental flow geometries could then be combined to form arbitrary global flows, and switched on command.

While the cilia design investigated in the present work focuses on cilia with two independently controlled hinges, one could imagine embedding more hinges into each cilium to generate larger nonreciprocity and more efficient pumping. In addition, adding diagonal hinges would allow for rotating the hinged cilium to enable a single cilium to pump in arbitrary directions. Thus, as with their biological counterparts, adding even more internal structure will enable greater functionality in the robotic cilia.

These micro fluidic manipulation abilities make the cilial platform highly desirable for incorporating with microfluidic and flow chemistry apparatuses where such cilia could provide fine adjustments, reprogrammable elements, that could enhance the capabilities of such apparatuses. When incorporated with circuits and sensors such cilia could respond automatically to local conditions to promote more efficient chemistries. One could even envision entire cilia metasurfaces that learn how to perform chemical reactions – transporting reactants, mixing them to facilitate reactions, and separating products – all on a cm scale chip. Finally, when untethered from the wafer, such cilia could be used to enable locomotion of microscopic robots. Here, sub mm robots with onboard CMOS circuits serving as their "brain" could make use of cilia with internal hinges to locomote through fluids in a manner similar to their biological counterparts.

4 Materials and methods

Fabrication and testing of artificial cilium

The fabrication process for artificial cilia, primarily utilizes photolithography and is outlined as follows (refer to Fig. 1A): 1) substrate preparation: silicon dioxide wafers are cleaned using hot piranha and serve as the substrate for the fabrication process. 2) Release layer deposition: a 180 nm layer of aluminum is deposited through E-beam evaporation (CVC SC4500), followed by a 30 nm aluminum oxide layer grown using atomic layer deposition (OXFORD ALD FlexAL). These layers act as the releasing layers. 3) Pattern formation for release layers: positive photoresist (Microposit S1813) is spin-coated onto the substrate and exposed using an ABM contact aligner. The exposed wafer is then developed by a suitable developer (MicroChemicals AZ 726 MIF) to get the pattern. 4) Etching of releasing layers: the exposed releasing layers undergo etching using an aluminum etchant (Aluminum Etchant Type A). 5) Photoresist stripping and cleaning: the photoresist is removed using an organic remover (Microposit Remover 1165) with sonication. Subsequently, the substrate undergoes oxygen plasma cleaning for 5 minutes (Oxford PlasmaLab 80+). 6) SiO_2 deposition: a 500 nm SiO_2 layer is grown using plasma-enhanced chemical vapor deposition (Oxford 100). 7) SiO_2 pattern formation: positive photoresist (Microposit S1813) is again spin-coated, exposed using an ABM contact aligner, and the exposed SiO_2 is etched using $CHF3/O_2$ (Oxford PlasmaLab 80+). 8) Photoresist stripping and cleaning: the photoresist is once again stripped using an organic remover (Microposit Remover 1165) with sonication. Following this, the substrate undergoes oxygen plasma cleaning for 5 minutes (Oxford PlasmaLab 80+). 9) Ti sputtering: a 3 nm Ti layer is sputtered onto the wafer at 3 mTorr and 400 W using an AJA sputter tool. 10) Pt layer deposition: a 7 nm thick Pt layer is grown using atomic layer deposition (Veeco Savannah ALD) at 175 °C. 11) Ti and Pt etching: positive photoresist (Microposit S1813) is spin-coated and exposed using an ABM contact aligner, and the exposed Ti and Pt layers are etched using ion milling at 600 V (AJA ion mill). 12) Final photoresist stripping: the final step involves stripping the remaining photoresist using an organic remover (Microposit Remover 1165) with sonication.

 This journal is © The Royal Society of Chemistry 2024

Open Access Article. Published on 22 August 2024. Downloaded on 9/11/2025 10:19:27 AM. This article is licensed under a Creative Commons Attribution-NonCommercial 3.0 Unported Licence.

The sample is released in a 5% TMAH solution. Subsequently, the solvent is transferred to phosphate-buffered saline (PBS; 1×; pH 7.45) to mimic the bio-environment. To initiate the actuation of the artificial cilium, a positive voltage of approximately 1 V relative to the Ag/AgCl reference electrode is applied to the cilia using the Pt/Ir probes. This voltage triggers electrochemical oxidation of the exposed Pt surface while effectively preventing bubble formation. As a result of this oxidation process, the Pt surface expands, causing the cilium to flatten. Reverting the actuator to its initial state involves applying a voltage of approximately −0.5 V, which reduces the Pt film. This voltage change effectively restores the artificial cilia to its original configuration. The process of fluid pumping is accomplished through the application of oscillating voltage signals from a function generator.

Pumping velocity measurement

We use an Olympus IX71 inverted microscope, integrated with a 3-axis micromanipulator from Sensapex and a video camera, to observe the actuation and pumping of artificial cilia. We track the fluid motion by introducing 2 μm polymer tracer particles into the solvent. The fluid velocity data reported in this study is based on the averaged velocity of these tracked particles.

Flow patterns from one cilia array

We get the flow pattern using the same Olympus IX71 inverted microscope. We use 2 μm yellow-green fluorescent particles (FluoSpheres™ Sulfate Microspheres) in combination with an optical filter to get the trajectories of these particles. The filter ensures that only the fluorescent particles are visible. We use MATLAB to process the video and only keep the florescent particles and get the images in Fig. 3.

The MATLAB PIVlab toolbox is used to process the images/videos with the fast Fourier transform cross correlation method.[27] The first pass uses a 128 pixel × 128 pixel interrogation window and the final window has a size of 16 pixel × 16 pixel with 50% overlap. The Gauss 2 × 3 point sub-pixel estimator is also used to improve the accuracy of PIV results.

Fabrication of CMOS integrated hinged cilium

The CMOS circuit is built on the SOI substrate from X-FAB. We grow cilium after receiving the chip from X-FAB. We describe the fabrication process as follows: 1) The SiO_2 layer on top of the CMOS circuit is first thinned by oxygen plasma etching (Oxford PlasmaLab 80+). 2) A 180 nm sputtered aluminum layers and a 30 nm ALD Al_2O_3 layer are deposited and patterned as release layers. 3) The electrical contacts are exposed by selectively etching the top SiO_2 layer. 4) Metal wires, made of Ti and Pt, are patterned to interconnect the CMOS circuit and artificial cilium using lift off. 5) A 500 nm SiO_2 insulation layer is then patterned on top of the CMOS circuit. 6) 300 nm chrome is patterned as the light shielding layer on top of the CMOS circuit, protecting the CMOS circuit from being exposed to the light and leaving the photovoltaics exposed to light. 7) Finally, the artificial cilia were fabricated following the recipe in the section titled Fabrication and testing of artificial cilium.

Theory and simulation

Model of a single cilium. To confirm the understanding of the physical mechanism behind hinged cilia actuation and to then gain insight into the features of the system that are difficult to record experimentally, a simple theoretical model was formulated. A cilium was modeled as a pair of slender, rigid rods with centrelines $\mathbf{r}_i(s, t)$, $i = 1, 2$, where t represents time and $s \in [0, L/2]$ the arclength, assuming rods are of equal length and L to be the total length of a cilium. Rod 1 is connected both to the substrate and rod 2 by a hinge equipped with a torsional spring, as illustrated in Fig. S5.† The shape of the cilium is then uniquely described by the two angles $\alpha_1(t)$, between the substrate and the rod number 1, and $\alpha_2(t)$, the angle between the two rods (see Fig. S5†). With the origin set at the point of connection to the substrate, the shape is then described mathematically by

$$\mathbf{r}_1(s, t) = s[\cos\alpha_1, \sin\alpha_1, 0]^T, \tag{1}$$

$$\mathbf{r}_2(s, t) = \frac{L}{2}[\cos\alpha_1, \sin\alpha_1, 0]^T + s[\cos(\alpha_1 + \alpha_2), \sin(\alpha_1 + \alpha_2), 0]^T, \tag{2}$$

with the axes oriented as in Fig. S5A.† Experimentally, the motion is driven by a periodic forcing of the elastic hinges. We model this as a preferred opening angle of the hinges *i.e.*, the equilibrium angle of the corresponding torsional springs

$$\hat{\alpha}_i(t) = \frac{\alpha_i^{\max} + \alpha_i^{\min}}{2} + \frac{\alpha_i^{\max} - \alpha_i^{\min}}{2}\operatorname{sign}[\sin(\omega t + \phi_i)],\ i = 1, 2; \tag{3}$$

where ω is the frequency of actuation, $\alpha_i^{\min}$ and $\alpha_i^{\max}$ the minimal and maximal value of the said angle, respectively, and ϕ_i the phase shift in the actuation. We set $\phi_1 = 0$, $\phi_2 = \pi/2$ to model the shape change as illustrated by the clockwise cycle in Fig. 1B ("pumping backward"). Torsional springs are then assumed to produce a torque

$$\tau_i = -\kappa_i[\alpha_i(t) - \hat{\alpha}_i(t)], \tag{4}$$

where the Hinge 1 connects the rod 1 to the substrate and the Hinge 2 connects the two rods, with the torques enumerated accordingly. Both hinges are produced in the same manner, thus we assume the torsional stiffness is the same for both $\kappa_1 = \kappa_2 = \kappa$. The model cilium is assumed to be surrounded by a Newtonian fluid of dynamic viscosity μ. Given the micro-sized length-scales of these cilia, it is justified to assume that the hydrodynamics are well

Open Access Article. Published on 22 August 2024. Downloaded on 9/11/2025 10:19:27 AM.
This article is licensed under a Creative Commons Attribution-NonCommercial 3.0 Unported Licence.

approximated by the low-Reynolds number dynamics. In particular, we neglect the inertia of the cilium and thus we can write the instantaneous force balance on each of the rods

$$\int_0^{L/2} \mathbf{f}(\mathbf{r}_1)\mathrm{d}s + \mathbf{F}_1 - \mathbf{F}_2 = 0, \tag{5}$$

$$\int_0^{L/2} \mathbf{f}(\mathbf{r}_2)\mathrm{d}s + \mathbf{F}_2 = 0, \tag{6}$$

where $\mathbf{f}(\mathbf{r})$ is the hydrodynamic drag experienced by the line element of the cilium at point r, the Hinge 1 acts with force $\mathbf{F}_1$ on rod 1 and hinge 2 acts with force $-\mathbf{F}_2$ or $\mathbf{F}_2$ on rods 1 and 2, respectively. Next, again due to neglecting the inertia, we can write the torque balance around each of the hinges as

$$\int_0^{L/2} \mathbf{r}_1(s,\,t) \times \mathbf{f}(\mathbf{r}_1)\mathrm{d}s - \mathbf{h}_2 \times \mathbf{F}_2 + \tau_1\hat{\mathbf{z}} = \mathbf{0}, \tag{7}$$

$$\int_0^{L/2} (\mathbf{r}_1(s,\,t) - \mathbf{h}_2) \times \mathbf{f}(\mathbf{r}_1)\mathrm{d}s + \int_0^{L/2} (\mathbf{r}_2(s,\,t) - \mathbf{h}_2) \times \mathbf{f}(\mathbf{r}_2)\mathrm{d}s - \mathbf{h}_2 \times \mathbf{F}_1 + \tau_2\hat{\mathbf{z}} = \mathbf{0}, \tag{8}$$

where $\hat{\mathbf{z}}$ is a unit vector corresponding to the third dimension of the system, pointing out of the page in ESI† Fig. S5A and $\mathbf{h}_2 = \mathbf{r}_1(L/2,\,t) = \mathbf{r}_2(0,\,t)$ is the location of the Hinge 2 connecting the two rods. After eliminating the contact forces $\mathbf{F}_1$ and $\mathbf{F}_2$ we get

$$\int_0^{L/2} \mathbf{r}_1(s,\,t) \times \mathbf{f}(\mathbf{r}_1)\mathrm{d}s + \mathbf{h}_2 \times \int_0^{L/2} \mathbf{f}(\mathbf{r}_2)\mathrm{d}s + \tau_1\hat{\mathbf{z}} = \mathbf{0}, \tag{9}$$

$$\int_0^{L/2} \mathbf{r}_1(s,\,t) \times \mathbf{f}(\mathbf{r}_1)\mathrm{d}s + \int_0^{L/2} \mathbf{r}_2(s,\,t) \times \mathbf{f}(\mathbf{r}_2)\mathrm{d}s + \tau_2\hat{\mathbf{z}} = \mathbf{0}, \tag{10}$$

Due to the assumption of low Reynolds number fluid flow, the fluid–structure interaction can be well modeled by the boundary integral equation[28] that in a case of a slender object with centreline $\mathbf{r}(s,\,t)$ near a plane wall[29,30] can be approximated to

$$\frac{\mathrm{d}}{\mathrm{d}t}\mathbf{r}(\tilde{s},\,s) = -\int \mathbf{B}[\mathbf{r}(t,\,\tilde{s});\,\mathbf{r}(t,\,s)]\cdot\mathbf{f}[\mathbf{r}(t,\,s)]\mathrm{d}s, \tag{11}$$

where $\mathbf{B}[\mathbf{r}(\tilde{s}),\,\mathbf{r}(s)]$ represents a well-known "blakelet" singularity tensor,[26] $\mathbf{r}(\tilde{s})$ due to a point force set at $\mathbf{r}(s)$ in the half-space bounded by a rigid plane wall. Together, eqn (4) and (9)–(11) represent a closed system of equations that yields a solution to our model. Before numerically approaching the problem, the system is non-dimensionalized by scaling lengths by the length of cilia L, torques by the torsional stiffness of springs κ and thus scaling forces by κL^{-1}. A characteristic time-scale $T = \mu L^3\kappa^{-1}$ arises from eqn (11) and represents a typical time-scale of the system for relaxation of any abrupt forcing introduced at the torsional springs. Hence, time is scaled by T while the actuation frequency is non-dimensionalized as $\bar{f} = \omega T = \omega\mu L^3\kappa^{-1}$. Note that, under the assumption that the Reynolds number vanishes, there is a single dimensionless parameter $\bar{f} = \omega\mu L^3\kappa^{-1}$ that describes the behaviour of the system. Apart from directly representing the dimensionless actuation frequency, this parameter is closely related to the well-known Sperm number.[31]

To numerically solve the problem, we will utilize the approach of regularized singularities.[32] This method regularizes the singular point-force singularities in eqn (11) to an algebraic blob of finite width ε thus only changing the "blakelet" tensor to its regularised version $\tilde{\mathbf{B}}[\mathbf{r}(\tilde{s}),\,\mathbf{r}(s),\,\varepsilon]$, as given in ref. 33. We discretise the each rod into $N = 50$ points $\mathbf{r}_i^j$, $j = 1,\,\ldots,\,N$ along the centreline. For simplicity, we will now drop the subscript denoting on which rod the point is and denote the points of discretization as $\mathbf{r}^j$, $j = 1,\,\ldots,\,2N$ with $\mathbf{f}^j$ the corresponding fluid drag forces. Eqn (11) is thus approximated to

$$\frac{\mathrm{d}\mathbf{r}^j}{\mathrm{d}t} = \mathbf{v}_1^j\dot{\alpha}_1 + \mathbf{v}_2^j\dot{\alpha}_2 = -\sum_j \mathbf{B}(\mathbf{r}^i;\,\mathbf{r}^j;\,\varepsilon)\cdot\mathbf{f}^j \tag{12}$$

where $\mathbf{v}_i^j$ is the unit velocities of the discretization points under rotations around the hinges, easily calculated from shape eqn (1) and (2). The regularization parameter ε is chosen as the half-length of a distance between the neighboring points under the said discretization. Assuming the motion of the cilium remains planar, the discretized version of governing equations represents a system of $4N + 2$ equations with the same number of variables, $2N$ force components, and rates of change of α_i. Inverting the system in eqn (12) is relatively simple when represented in matrix form and thus it can be used to express forces in terms of $\dot{\alpha}_i$ and substitute in torque balance equations, resulting in a simple 2 by 2 system of equations for the angular rates of change. After solving this system at each time-step we evolve the system by using a simple first-order explicit Euler method.

Flow simulations. The flow around arrays of cilia is simulated by approximating the flow generated by each cilium by that of a point-force of strength F set at height $0.7L$ above the substrate, where L is the length of each cilium. The force intensity and location is kept constant for each cilium as it represents the time-averaged effect over multiple periods of actuation in order to simulate the time-averaged flows. Flow due to each point-force is first adjusted to the presence of the rigid substrate[26] and the full flow is then obtained through the superposition of all the point-force flows. Such a superposition is valid due to the linearity of the Stokes equations that govern the fluid dynamics in this case. All the velocities presented in this paper that resulted from these simulations are non-dimensionalized by the factor of $F/L\mu$, where μ is the dynamic viscosity of the surrounding fluid. Computation of the flow is performed on a rectangular grid mirroring the experimental field of view horizontally, with the vertical axis spanning from $0.8L$ to $4L$. To

 This journal is © The Royal Society of Chemistry 2024

Open Access Article. Published on 22 August 2024. Downloaded on 9/11/2025 10:19:27 AM.
This article is licensed under a Creative Commons Attribution-NonCommercial 3.0 Unported Licence.

illustrate 2D streamlines in comparison to experimental data, we create a compressible 2D flow by averaging the 3D flow over its height above the surface.

Data availability

All data needed to evaluate the conclusions in the paper are present in the paper or the ESI.†

Author contributions

W. W., and I. C. conceived of the experiments. W. W. designed and fabricated the cilia, carried out the experiments. W. W. and J. Z. analyzed the data. I. T. and E. L. conducted all of the simulations to determine the pumping performance and flow trajectories. W. W. and I. C. wrote the manuscript with all authors contribution.

Conflicts of interest

I. C. is the inventor of a patent application (PCT/US2021/021419) submitted by Cornell University that covers electrically programmable microscale shape-memory actuators and related robotic devices. W. W. and I. C. are inventors on a provisional patent application (63/267190) submitted by Cornell University that covers actuators and control electronics for cilia metasurfaces and a provisional patent application (63/368751) submitted by Cornell University that covers integrated circuits for controlling microscopic robots. The other authors declare no competing interests.

Acknowledgements

This work was supported by the Army Research Office (ARO W911NF-18-1-0032), the National Science Foundation (EFMA-1935252, and FRR-2325585) the Cornell Center for Materials Research (DMR-1719875), and the Kavli Institute at Cornell for Nanoscale Science. This work was performed in part at Cornell NanoScale Facility, an NNCI member supported by NSF Grant NNCI-2025233. We thank for valuable discussions, Alyssa Apsel, Milad Taghavi, and Parag Chaudhari, and Tom Pennell, Jeremy Clark, and Garry Bordonaro for technical support.

References

1 G. I. Taylor, *Proc. R. Soc. London, Ser. A*, 1951, **209**, 447–461.
2 E. Lauga and T. R. Powers, *Rep. Prog. Phys.*, 2009, **72**, 096601.
3 E. Lauga, *The fluid dynamics of cell motility*, Cambridge University Press, 2020, vol. 62.
4 C. Brennen and H. Winet, *Annu. Rev. Fluid Mech.*, 1977, **9**, 339–398.
5 H. C. Berg and R. A. Anderson, *Nature*, 1973, **245**, 380–382.
6 M. King, A. Gilboa, F. Meyer and A. Silberberg, *Am. Rev. Respir. Dis.*, 1974, **110**, 740–745.
7 M. Vilfan, A. Potočnik, B. Kavčič, N. Osterman, I. Poberaj, A. Vilfan and D. Babič, *Proc. Natl. Acad. Sci. U. S. A.*, 2010, **107**, 1844–1847.
8 X. Dong, G. Z. Lum, W. Hu, R. Zhang, Z. Ren, P. R. Onck and M. Sitti, *Sci. Adv.*, 2020, **6**, eabc9323.
9 T. ul Islam, Y. Wang, I. Aggarwal, Z. Cui, H. E. Amirabadi, H. Garg, R. Kooi, B. B. Venkataramanachar, T. Wang and S. Zhang, *et al.*, *Lab Chip*, 2022, **22**, 1650–1679.
10 J. den Toonder, F. Bos, D. Broer, L. Filippini, M. Gillies, J. de Goede, T. Mol, M. Reijme, W. Talen and H. Wilderbeek, *et al.*, *Lab Chip*, 2008, **8**, 533–541.
11 S. Peerlinck, E. Milana, E. De Smet, M. De Volder, D. Reynaerts and B. Gorissen, *Adv. Funct. Mater.*, 2023, 2300856.
12 S. Zhang, X. Hu, M. Li, U. Bozuyuk, R. Zhang, E. Suadiye, J. Han, F. Wang, P. Onck and M. Sitti, *Sci. Adv.*, 2023, **9**, eadf9462.
13 M. Z. Miskin, A. J. Cortese, K. Dorsey, E. P. Esposito, M. F. Reynolds, Q. Liu, M. Cao, D. A. Muller, P. L. McEuen and I. Cohen, *Nature*, 2020, **584**, 557–561.
14 Q. Liu, W. Wang, M. F. Reynolds, M. C. Cao, M. Z. Miskin, T. A. Arias, D. A. Muller, P. L. McEuen and I. Cohen, *Sci. Robot.*, 2021, **6**(52), eabe6663.
15 W. Wang, Q. Liu, I. Tanasijevic, M. F. Reynolds, A. J. Cortese, M. Z. Miskin, M. C. Cao, D. A. Muller, A. C. Molnar and E. Lauga, *et al.*, *Nature*, 2022, **605**, 681–686.
16 T. Ishikawa, *Cold Spring Harbor Perspect. Biol.*, 2017, **9**, a028076.
17 H. C. Berg, *Annu. Rev. Biochem.*, 2003, **72**, 19–54.
18 R. M. Macnab, *Proc. Natl. Acad. Sci. U. S. A.*, 1977, **74**, 221–225.
19 N. C. Darnton and H. C. Berg, *Biophys. J.*, 2007, **92**, 2230–2236.
20 Y. Hyon, T. R. Powers, R. Stocker and H. C. Fu, *et al.*, *J. Fluid Mech.*, 2012, **705**, 58–76.
21 Y. Katsu-Kimura, F. Nakaya, S. A. Baba and Y. Mogami, *J. Exp. Biol.*, 2009, **212**, 1819–1824.
22 K. Bouhouche, M. Valentine, P. Le Borgne, M. Lemullois, J. Yano, S. Lodh, A. Nabi, A. Tassin and J. Van Houten, *Front. Cell Dev. Biol.*, 2022, **10**, 847908.
23 E. M. Purcell, *Am. J. Physiol.*, 1977, **45**, 3–11.
24 K. E. Machin, *J. Exp. Biol.*, 1958, **35**, 796–806.
25 C. H. Wiggins and R. E. Goldstein, *Phys. Rev. Lett.*, 1998, **80**, 3879–3882.
26 J. R. Blake, *Math. Proc. Cambridge Philos. Soc.*, 1971, **70**, 303–310.
27 W. Thielicke and R. Sonntag, *J. Open Res. Softw.*, 2021, **9**(1), 12.
28 C. Pozrikidis, *Boundary integral and singularity methods for linearized viscous flow*, Cambridge university press, 1992.
29 D. F. Katz, J. R. Blake and S. Paveri-Fontana, *J. Fluid Mech.*, 1975, **72**, 529–540.
30 L. Koens and E. Lauga, *J. Fluid Mech.*, 2018, **850**, R1.
31 R. Dreyfus, J. Baudry, M. L. Roper, M. Fermigier, H. A. Stone and J. Bibette, *Nature*, 2005, **437**, 862–865.
32 R. Cortez, *SIAM J. Sci. Comput.*, 2001, **23**, 1204–1225.
33 R. Cortez and D. Varela, *J. Comput. Phys.*, 2015, **285**, 41–54.